

1 **Long term variations of actual evapotranspiration over the Tibetan**
2 **Plateau**

3 Cunbo Han ^{1,2,3}, Yaoming Ma ^{1,4,5,6}, Binbin Wang ^{1,2}, Lei Zhong ⁷, Weiqiang

4 Ma ^{1,2,4}, Xuelong Chen ^{1,2,4}, Zhongbo Su ⁸

5 1. Key Laboratory of Tibetan Environment Changes and Land Surface
6 Processes, Institute of Tibetan Plateau Research, Chinese Academy of
7 Sciences, Beijing, China

8 2. Land-Air Interaction and Climate Effect Group, State Key Laboratory of
9 Tibetan Plateau Earth System Science, Institute of Tibetan Plateau
10 Research, Chinese Academy of Sciences, Beijing, China

11 3. Institute for Meteorology and Climate Research, Karlsruhe Institute of
12 Technology, Karlsruhe, Germany

13 4. CAS Center for Excellence in Tibetan Plateau Earth Sciences, Chinese
14 Academy of Sciences, Beijing, China

15 5. University of Chinese Academy of Sciences, Beijing, China

16 6. Lanzhou University, Lanzhou, China

17 7. Laboratory for Atmospheric Observation and Climate Environment
18 Research, School of Earth and Space Sciences, University of Science
19 and Technology of China, Hefei, China

20 8. Faculty of Geo-Information Science and Earth Observation, University of
21 Twente, Enschede, The Netherlands

22

23 **Correspondence to:**

24 Prof. Dr. Yaoming Ma

25 Institute of Tibetan Plateau Research, Chinese Academy of Sciences

26 16-3 Lincui Road, Chaoyang District, Beijing, 100101, China

27 Tel: +86 010 84097079

28 Email: ymma@itpcas.ac.cn

Deleted: ³,

Deleted: ⁶

Deleted: ³

Deleted: ³

Deleted: ⁷

Deleted: Chinese Academy of Sciences,

Deleted: (ITPCAS)

Deleted: ¶

Deleted: ¶

38 **Abstract**

39 Terrestrial actual evapotranspiration (ET_a) is a key parameter controlling land-
40 atmosphere interaction processes and the water cycle. However, the spatial
41 distribution and temporal changes of ET_a over the Tibetan Plateau (TP)
42 remain very uncertain. Here we estimate the multiyear (2001-2018) monthly
43 ET_a and its spatial distribution on the TP by a combination of meteorological
44 data and satellite products. Validation against data from six eddy-covariance
45 monitoring sites yielded root-mean-square errors ranging from 9.3 to 14.5 mm
46 mo^{-1} , and correlation coefficients exceeding 0.9. The domain mean of annual
47 ET_a on the TP decreased slightly (-1.45 mm yr^{-1} , $p < 0.05$) from 2001 to 2018.
48 The annual ET_a increased significantly at a rate of 2.62 mm yr^{-1} ($p < 0.05$) in
49 the eastern sector of the TP ($lon > 90^\circ\text{ E}$), but decreased significantly at a rate
50 of -5.52 mm yr^{-1} ($p < 0.05$) in the western sector of the TP ($lon < 90^\circ\text{ E}$). In
51 addition, the decreases in annual ET_a were pronounced in spring and summer
52 seasons, while almost no trends were detected in the autumn and winter
53 seasons. The mean annual ET_a during 2001-2018 and over the whole TP was
54 $496 \pm 23\text{ mm}$. Thus, the total evapotranspiration from the terrestrial surface of
55 the TP was $1238.3 \pm 57.6\text{ km}^3\text{ yr}^{-1}$. The estimated ET_a product presented in
56 this study is useful for an improved understanding of changes in energy and
57 water cycle on the TP. The dataset is freely available at the Science Data
58 Bank (<http://www.dx.doi.org/10.11922/sciencedb.t00000.00010>, (Han et al.,
59 [2020](#))) and at the National Tibetan Plateau Data Center
60 (<https://data.tpdac.ac.cn/en/data/5a0d2e28-ebc6-4ea4-8ce4-a7f2897c8ee6/>).

61

62 **Key words:** Actual evapotranspiration; SEBS; Tibetan Plateau; Trend.

63

Deleted: the

Deleted: a

Deleted:

Deleted:

68

69 **Key points:**

- 70 • The SEBS-estimated monthly ET_a during 2001-2018 has been
71 validated against 6 flux towers on the TP.
- 72 • Annual ET_a over the entire TP and in the western TP decrease
73 significantly, while it increases in the eastern TP.
- 74 • Decrease of annual ET_a is pronounced in spring and summer, while
75 almost no trends are detected in autumn and winter.

76

77

Deleted: shows acceptable accuracy

79 **1 Introduction**

80 As the birthplace of Asia's major rivers, the Tibetan Plateau (TP), famous as
81 the "Water Tower of Asia", is essential to the Asian energy and water cycles
82 ([Immerzeel et al., 2010](#); [Yao et al., 2012](#)). Along with increasing air
83 temperature, evidence from the changes of precipitation, runoff, and soil
84 moisture indicates that the hydrological cycle of the TP has been intensified
85 during the past century ([Yang et al., 2014](#)). ~~Consuming~~ around two-thirds of
86 global terrestrial precipitation, evapotranspiration (*ET*) is a crucial component
87 that affects the exchange of water and energy between the land surface and
88 the atmosphere ([Oki and Kanae, 2006](#); [Fisher et al., 2017](#)). *ET* is also a ~~key~~,
89 factor modulating regional and global weather and climate. As ~~one essential~~,
90 connecting component between the energy budget and the water cycle in the
91 terrestrial ecosystems ([Xu and Singh, 2005](#)), *ET* and ~~its~~ variations ~~have been~~
92 ~~drawing more~~ attention worldwide ([Xu and Singh, 2005](#); [Li et al., 2014](#); [Zhang](#)
93 [et al., 2018b](#); [Yao et al., 2019](#); [Wang et al., 2020b](#)). Total evaporation from
94 large lakes of the TP has been quantitatively estimated recently ([Wang et al.,](#)
95 [2020a](#)), however, the terrestrial *ET* on the TP and its spatial and temporal
96 changes remain very uncertain.

97
98 Many studies have tried to evaluate *ET*'s temporal and spatial variability
99 across the TP using various methods. The pan evaporation (E_{pan}), that
100 represents the amount of water evaporated from an open circular pan, is the
101 most popular observational data source of *ET*. Long time series of E_{pan} are
102 often available with good comparability among various regional
103 measurements. Thus, it has been widely used in various disciplines, e.g.,
104 meteorology, hydrology, and ecology. Several studies have revealed the trend
105 of E_{pan} on the TP ([Zhang et al., 2007](#); [Liu et al., 2011](#); [Shi et al., 2017](#); [Zhang](#)
106 [et al., 2018a](#); [Yao et al., 2019](#)). Although E_{pan} and potential *ET* suggest the

Deleted: Contributing

Deleted: n essential

Deleted: the

Deleted: only

Deleted: of *ET* over the TP

Deleted: received increasing

113 long-term variability of ET according to [the complementary relationship \(CR\)](#),
114 between E_{pan} and actual ET (ET_a) ([Zhang et al., 2007](#)), these measures
115 cannot precisely depict the spatial pattern of trends in ET_a . Recently, several
116 studies applied revised models, which are based on the [CR of \$ET\$](#) , to estimate
117 ET_a on the TP ([Zhang et al., 2018b](#); [Ma et al., 2019](#); [Wang et al., 2020b](#)).
118 Employing only routine meteorological observations without requiring any
119 vegetation and soil information is the most significant advantage of CR
120 models ([Szilagyi et al., 2017](#)). However, numerous assumptions and
121 requirements of validations of key parameters limit the application and
122 performance of CR models over different climate conditions. The application
123 of eddy-covariance (EC) technologies in the past decade has dramatically
124 advanced our understanding of the terrestrial energy balance and ET_a over
125 various ecosystems across the TP. However, the fetch of the EC observation
126 is on the order of hundreds of meters, thus impeding the ability to capture the
127 plateau-scale variations of ET_a . Therefore, finding an effective way to advance
128 the estimation of ET_a on the TP is of great importance.

129

130 Satellite remote sensing (RS) provides temporally frequent and spatially
131 contiguous measurements of land surface characteristics that affect ET , for
132 example, land surface temperature, albedo, vegetation index. Satellite RS
133 also offers the opportunity to retrieve ET over a heterogeneous surface
134 ([Zhang et al., 2010](#)). Multiple RS-based algorithms have been proposed.
135 Among these algorithms, the surface energy balance system (SEBS)
136 proposed by [Su \(2002\)](#) has been widely applied to retrieve land surface
137 turbulent fluxes on the TP ([Chen et al., 2013b](#); [Ma et al., 2014](#); [Han et al.,](#)
138 [2016](#); [Han et al., 2017](#); [Zou et al., 2018](#); [Zhong et al., 2019](#)). [Chen et al.](#)
139 [\(2013b\)](#) improved the roughness length parameterization scheme for heat
140 transfer in SEBS to expand its modeling applicability over bare ground, sparse

Deleted: contrasting trends

Deleted: complementary relationship (

Deleted:)

144 canopy, dense canopy, and snow surfaces in the TP. An algorithm for effective
145 aerodynamic roughness length had been introduced into the SEBS model to
146 parameterize subgrid-scale topographical form drag ([Han et al., 2015](#); [Han et
147 al., 2017](#)). This scheme improved the skill of the SEBS model in estimating
148 the surface energy budget over mountainous regions of the TP. A recent
149 advance by [Chen et al. \(2019\)](#) optimized five critical parameters in SEBS
150 using observations collected from 27 sites globally, including 6 sites on the TP,
151 and suggested that the overestimation of the global ET was substantially
152 improved with the use of optimal parameters.

153

154 While the spatial and temporal pattern of the ET_a in the TP had been
155 investigated in many studies ([Zhang et al., 2007](#); [Zhang et al., 2018b](#); [Wang
156 et al., 2020b](#)), considerable inconsistencies for both trends and magnitudes of
157 ET_a exist due to uncertainties in forcing and parameters used by various
158 models. Thus, in this study, with full consideration of the recent developments
159 in the SEBS model over the TP, we aim to (1) develop an 18-year (2001-2018)
160 ET_a product of the TP, along with independent validations against EC
161 observations; (2) quantify the spatiotemporal variability of the ET_a in the TP,
162 and (3) uncover the main factors dominating the changes in ET_a , using the
163 estimated product.

164

165 **2 Methodology and data**

166 **2.1 Model description**

167 The SEBS model ([Su, 2002](#)) was used to derive land surface energy flux
168 components in the present study. The remote-sensed land surface energy
169 balance equation is given by

170
$$R_n = H + LE + G_0. \quad (1)$$

171 R_n is net radiation flux ($W\ m^{-2}$), H is sensible heat flux ($W\ m^{-2}$), LE is latent
 172 heat flux ($W\ m^{-2}$), and G_0 is ground heat flux ($W\ m^{-2}$). Note that this equation
 173 neglected energy stored in the canopy, energy consumption related to freeze-
 174 thaw processes of permafrost and glacier, etc. Thus, this equation is
 175 applicable without considering the phase change of water.

Deleted: the
 Deleted: the
 Deleted: the
 Deleted: the

176
 177 The land surface net radiation flux was computed as

178
$$R_n = (1 - \alpha) \times SWD + LWD - \varepsilon \times \sigma \times T_s^4 \quad (2)$$

179 where α is the land surface albedo derived from the Moderate Resolution
 180 Imaging Spectroradiometer (MODIS) products. Downward shortwave (SWD)
 181 and longwave (LWD) radiation were obtained from the China Meteorological
 182 Forcing Dataset (CMFD). Land surface temperature (T_s) and emissivity (ε)
 183 values were also obtained from MODIS products.

184

185 In vegetated areas the soil heat flux, G_0 , was calculated from the net radiation
 186 flux and vegetation cover

187
$$G_0 = R_n \times (r_c \times f_c + r_s \times (1 - f_c)). \quad (3)$$

188 r_s and r_c are ratios of ground heat flux and net radiation for surfaces with bare
 189 soil and full vegetation, respectively. Fractional vegetation cover (f_c) was
 190 derived from the normalized difference vegetation index (NDVI). Over water
 191 surfaces (NDVI < 0 and $\alpha < 0.47$), $G_0 = 0.5R_n$ was used ([Gao et al., 2011](#);
 192 [Chen et al., 2013a](#)). On glaciers, G_0 is negligible ([Yang et al., 2011](#)) and $G_0 =$
 193 $0.05R_n$.

194

195 In the atmospheric surface layer, sensible heat flux and friction velocity were
 196 calculated based on the Monin-Obukhov similarity ([Stull, 1988](#)),

197
$$U = \frac{u_*}{\kappa} \left[\ln \left(\frac{z-d_0}{z_{om}^{eff}} \right) - \psi_m \left(\frac{z-d_0}{L} \right) + \psi_m \left(\frac{z_{om}^{eff}}{L} \right) \right] \quad (4)$$

$$\theta_0 - \theta_a = \frac{H}{\kappa u_* \rho C_p} \left[\ln \left(\frac{z-d_0}{z_{0h}^{eff}} \right) - \psi_h \left(\frac{z-d_0}{L} \right) + \psi_h \left(\frac{z_{0h}^{eff}}{L} \right) \right] \quad (5)$$

$$L = \frac{\rho C_p u_*^2 \theta_v}{\kappa g H} \quad (6)$$

204 U is the horizontal wind velocity at a reference height z (m) above the ground
 205 surface, θ_0 is the potential temperature at the land surface (K), θ_a is the
 206 potential temperature (K) at the reference height z , d_0 is the zero-plane
 207 displacement height (m), ρ is the air density (kg m^{-3}), C_p is the specific heat for
 208 moist air ($\text{J kg}^{-1} \text{ }^\circ\text{C}^{-1}$), $\kappa = 0.4$ is the von Kármán's constant, u_* is the friction
 209 velocity, L is the Monin-Obukhov length (m), θ_v is the potential virtual
 210 temperature (K) at the reference height z , ψ_m and ψ_h are the stability
 211 correction functions for momentum and sensible heat transfer respectively,
 212 and g is the gravity acceleration (m s^{-2}). To account for the form drag caused
 213 by subgrid-scale topographical obstacles, effective roughness lengths for
 214 momentum (z_{0m}^{eff} , m) and sensible heat (z_{0h}^{eff} , m) transfer were introduced into
 215 the SEBS model by [Han et al. \(2017\)](#). These modifications are parameterized
 216 as follows ([Grant and Mason, 1990](#); [Han et al., 2015](#)),

$$\ln^2 \left(\frac{h/2z_{0m}^{eff}}{0.5D\lambda + \kappa^2 / \ln^2(h/2z_{0m})} \right) = \frac{\kappa^2}{0.5D\lambda + \kappa^2 / \ln^2(h/2z_{0m})} \quad (7)$$

$$\ln \left(\frac{h/2z_{0h}^{eff}}{\ln(h/2z_{0h} + 1)} + 1 \right) = \ln \left(\frac{h/2z_{0h} + 1}{\ln(h/2z_{0h} + 1)} \right) \frac{\ln(h/2z_{0m} + 1)}{\ln(h/2z_{0m}^{eff} + 1)} \quad (8)$$

219 where h is the average height of the subgrid-scale roughness obstacles, λ is
 220 the average density of the subgrid-scale roughness elements calculated from
 221 digital elevation models, D is the form drag coefficient and $D=0.4$ is used for
 222 the mountainous areas of the TP as suggested by [Han et al. \(2015\)](#), z_{0m} and
 223 z_{0h} are the local-scale roughness lengths for momentum (m) and heat transfer
 224 (m), respectively. Detailed calculations can be found in [Su \(2002\)](#). A revised
 225 algorithm for z_{0h} developed by [Chen et al. \(2013b\)](#) was applied as this
 226 algorithm outperforms the original scheme of the SEBS model on the TP.

227

228 To constraint the actual evapotranspiration, the evaporative fraction was

Formatted: Font: Italic

Deleted: an

230 applied in the SEBS model, which is determined by taking energy balance
231 considerations at dry and wet limiting cases. Under the dry-limit condition, the
232 evaporation becomes zero due to the limited supply of available soil moisture,
233 while water vapor evaporates at the potential rate under the wet-limit condition
234 (Su, 2002). The evaporative fraction (Λ) is defined as,

235
$$\Lambda = \frac{LE}{R_n - G_0} \quad (9)$$

236 After calculating evaporative fraction based on the assumption of dry and wet
237 limits, latent heat flux was calculated by inverting Equation (9). Finally, latent
238 heat flux was converted to ET_a . Details are available in Su (2002) and (Chen
239 et al., 2013a).

240 2.2 Data

241 In-situ observations, satellite-based products, and meteorological forcing data
242 were used in this study to estimate monthly ET_a over the TP area. The CMFD,
243 that was developed based on the released China Meteorological
244 Administration (CMA) data (He et al., 2020), was used as model input. The
245 CMFD covers the whole landmass of China at a spatial resolution of 0.1° and
246 a temporal resolution of three hours. The CMFD dataset was established
247 through the fusion of in-situ observations, remote sensing products, and
248 reanalysis datasets. In particular, the dataset benefits from the merging of the
249 observations at about 700 CMA's weather stations, and by using the Global
250 Energy and Water Cycle Experiment – Surface Radiation Budget (GEWEX-
251 SRB) shortwave radiation dataset (Pinker and Laszlo, 1992). The GEWEX-
252 SRB data has not been used in any other reanalysis dataset. In addition,
253 independent datasets observed in western China where weather stations are
254 scarce were used to evaluate the CMFD. This includes data collected through
255 the Heihe Watershed Allied Telemetry Experimental Research (HiWATER) (Li
256 et al., 2013) and the Coordinated Enhanced Observing Period (CEOP) Asia-

Formatted: Font: Arial

Formatted: 公式1

Deleted: Finally, da

Deleted: ily ET_a

Deleted: using the evaporative fraction as a residual of the surface energy budget equation while accounting for dry and wet limits

Formatted: Font: Italic

Formatted: Subscript

262 Australia Monsoon Project (CAMP) ([Ma et al., 2003](#)). CMFD dataset has been
263 validated against in situ meteorological observations and compared with other
264 reanalysis datasets on the TP, demonstrating that it is one of the best
265 meteorological forcing datasets over the TP area ([Zhou et al., 2016](#); [Xie et al.,](#)
266 [2017](#); [Wang et al., 2020a](#)). Therefore, it is suitable for this study to drive the
267 SEBS model. Detailed information for the CMFD dataset is listed in [Table 1](#),
268
269 MODIS monthly land surface products, including land surface temperature
270 and emissivity, land surface albedo, and vegetation index, provide land
271 surface conditions for the SEBS model. Detailed information on MODIS land
272 surface variables are listed in Table 1. The values of land surface variables in
273 the MODIS monthly products are derived by compositing and averaging the
274 values from the corresponding month of MODIS daily files. Validations of
275 MODIS land surface temperature and albedo against in-situ observations on
276 the TP suggesting a high quality of MODIS land surface products with low
277 biases and small root-mean-square errors ([Wang et al., 2004](#); [Ma et al., 2011](#);
278 [Chen et al., 2014](#)).

Deleted: CMFD dataset is suitable for our study due to its continuous-time coverage and consistent quality.

Deleted: Table 1

279
280 In-situ EC data observed at six flux stations on the TP were used to validate
281 model results. Locations of the six observation sites are illustrated in [Figure 1](#),
282 and detailed descriptions for these six sites are shown in [Table 2](#). The
283 instrumental setup at each site consists of: an EC system comprising a sonic
284 anemometer (CSAT3, Campbell Scientific Inc) and an open-path gas analyzer
285 (LI-7500, Li-COR); a four-component radiation flux system (CNR-1, Kipp &
286 Zonen), installed at a height of 1.5 m; a soil heat flux plate (Hukseflux,
287 HFP01), buried in the soil to a depth of 0.1 m; soil moisture and temperature
288 probes, buried at a depth of 0.05, 0.10, and 0.15 m, respectively ([Han et al.,](#)
289 [2017](#)). The EC data were processed with the EC software package TK3

Deleted: Figure 1

Deleted: Table 2

295 ([Mauder and Foken, 2015](#)). The main post-processing procedures of the EC
296 raw data were as follows: spike detection, coordinate rotation, spectral loss
297 correction, frequency response corrections ([Moore, 1986](#)), and corrections for
298 density fluctuations ([Webb et al., 1980](#)). The ground heat flux was obtained by
299 summing the flux value observed by the heat flux plate and the energy
300 storage in the layer above the heat flux plate ([Han et al., 2016](#)). A more
301 comprehensive dataset including the EC data used in this work has been
302 published and is freely available ([Ma et al., 2020](#)).

Deleted: Monthly EC data, which are used for validation, were generated from half-hourly variables.

303
304 3-hourly CMFD data was averaged into daily and then into monthly data to be
305 consistent with MODIS products in terms of temporal resolution. Daily land
306 surface albedo has been averaged into monthly variable. MODIS land surface
307 products and canopy height data were remapped onto CMFD's grid. Monthly
308 EC data and in situ meteorological observations, which are used for model
309 validation, were generated from half-hourly variables.

310 2.3 Model evaluation metrics and data analysis methods

311 The model performance was assessed using the Pearson correlation
312 coefficient (R), the root-mean-square error (RMSE), and the mean bias (MB)
313 between the estimated and observed monthly ET_a at the six stations on the
314 TP.

Deleted:

Deleted:

315
316 The least-square regression technique was used to detect the long-term linear
317 annual trends in ET_a values. The linear model to simulate ET_a values (Y_t)
318 against time (t) is defined as below and the slope of the linear equation (b) is
319 taken as the changing trend.

Formatted: Font: Italic

$$320 Y_t = Y_0 + bt + \varepsilon_t$$

(10)

Deleted: 9

321

327 The Student's *t*-test, having an $n-2$ degree of freedom (n is the number of
328 samples), was used to evaluate the statistical significance of the linear
329 trends, and only tests with a p -value less than 0.05 were selected as having
330 passed the significance test.

331 3 Results and discussion

332 3.1 Validation against flux tower observations

333 The SEBS-estimated ET_a was validated against EC observations at six flux
334 stations on the TP at a monthly scale (Figure 2). The SEBS model is capable
335 of capturing both the magnitude and seasonal variation of the monthly ET_a
336 signal at all the six stations. The correlation coefficients are all larger than 0.9
337 and have passed the significance test at the $p = 0.01$ level. RMSE values
338 range from 9.3 to 14.5 mm mo⁻¹ with the minimum at the BJ station and the
339 maximum at the SETORS station. The MB values are all negative except at
340 the NADORS station, which means the SEBS model slightly underestimated
341 ET_a values on the TP.

342
343 Specifically, the SEBS model performed particularly well at the short grass
344 sites (BJ and NAMORS), with correlation coefficients as high as 0.98 and MB
345 values below 5.0 mm mo⁻¹. At the high grass site (SETORS) and the gravel
346 site (QOMS), the SEBS model is capable of reproducing the EC-observed
347 monthly ET_a with RMSE values of 14.5 and 13.2 mm mo⁻¹, respectively. In
348 addition, the underestimates of ET_a by SEBS are mostly in the dry season,
349 when the canopy is withered. The validation at the site-scale indicates that the
350 SEBS model used in this work can be applied to a wide range of ecosystems
351 over the TP.

Deleted: the

Deleted: Figure 2

Deleted: phase

Deleted: the spare grass stations (NADORS and MAWORS) and at

Formatted: Superscript

357 **3.2 Spatial distribution**

358 There was a clear spatial pattern to the multiyear average of annual ET_a
359 between 2001 and 2018 (Figure 3). In general, the SEBS-estimated ET_a
360 decreases from the southeast to the northwest of the TP, with the maximum
361 value above 1200 mm in the southeastern Tibet and Hengduan Mountains
362 and the minimum value less than 100 mm in the northwestern edge of the TP.
363 In the central TP, where there are several lakes, ET_a was typically from 500 to
364 1000 mm. ET_a was lower than 200 mm over the high, snow- and ice-bound,
365 mountainous areas. For example, over the northern slopes of the Himalaya,
366 Nyenchen Tanglha Mountains, and the eastern section of the Tanggula
367 Mountains. The reason is that these snow- and ice-bound mountainous areas
368 have a higher ability to reflect downward shortwave radiation and hence have
369 less available energy to evaporate. On the whole, the domain averaged
370 multiyear mean annual ET_a over the TP is 496 ± 23 mm. The total amount of
371 water evapotranspired from the terrestrial surface of the TP are around
372 1238.3 ± 57.6 km³ yr⁻¹, considering the area of the TP to be 2.5×10^6 km².

373
374 Figure 4 shows the multi-year average spring (Marth, April, and May), summer
375 (June, July, and August), autumn (September, October, and November), and
376 winter (December, January, and February) ET_a on the TP. Generally, the
377 distribution pattern of seasonal ET_a was comparable with that of the annual
378 ET_a . Both seasonal and annual ET_a show a decreasing trend from the
379 southeastern TP to the northwestern TP. Note that the spatial contrast of ET_a
380 almost faded out in winter season owing to a minimum in available energy
381 and precipitation (Figure 4d). The ET_a in spring is higher than that in autumn,
382 except for some high mountainous areas (e.g.: mountain ranges of Himalaya
383 and Hengduan mountains). The spring ET_a ranges from 50 mm to 450 mm,
384 while autumn ET_a ranges from 50 mm to 250 mm. In summer, the ET_a is

Deleted: multiyear (2001-2018) mean

Deleted: Figure 3

Deleted: Figure 4

Formatted: Font: Italic

Formatted: Subscript

Deleted: distribution pattern

Deleted: Figure 4

390 larger than 250 mm in most of the TP, while the ET_a is still below 100 mm in
391 large areas of the northwestern TP. The multiyear seasonal ET_a averaged
392 over the whole TP is 140 ± 10 mm, 256 ± 12 mm, 84 ± 5 mm, and 34 ± 4 mm, for
393 spring, summer, autumn, and winter, respectively.

394 3.3 Trend analysis

395 The trend of annual ET_a during 2001-2018 is shown in Figure 5. Overall, an
396 increasing trend of SEBS-simulated ET_a is dominant in the eastern TP (lon >
397 90° E) while a decreasing trend is dominant in the western TP (lon < 90° E).
398 The trends pass the t -test ($p < 0.05$) in most part of the areas. The decreasing
399 trend in the western TP is pronounced and passes the t -test ($p < 0.05$). This
400 trend is larger than -7.5 mm yr^{-1} in most parts of the area and even larger than
401 -10 mm yr^{-1} in a few parts. In the eastern TP, the increasing trend is mostly
402 between 5 and 10 mm yr^{-1} and passes the t -test ($p < 0.05$). The ET_a trend
403 tends to be greater along the marginal region of the northern, eastern, and
404 southeastern TP. Along the marginal region of the southwestern TP and in the
405 western section of Himalaya Mountains this trend weakens.

406

407 The trends of seasonal ET_a between 2001 and 2018 are spatially
408 heterogeneous over the TP (Figure 6). Decreasing trends in spring and
409 summer are generally at a rate between -2.5 and -7.5 mm yr^{-1} , and increasing
410 trends are generally at a rate below 5.0 mm yr^{-1} and 7.5 mm yr^{-1} in spring and
411 summer, respectively. Areas showing decreasing ET_a tend to become larger in
412 autumn and winter seasons. Both the decreasing and increasing trends are
413 subdued in autumn and winter compared with that in spring and summer
414 seasons. Decreasing rates of ET_a in autumn and winter are generally below -
415 2.5 mm yr^{-1} , and only a few areas have a rate larger than -2.5 mm yr^{-1} .

416

417 Due to the contrast in the trends in the eastern and western halves of the TP,
418 we divided the TP into two regions: the eastern TP ($\text{lon} > 90^\circ \text{ E}$) and the
419 western TP ($\text{lon} < 90^\circ \text{ E}$). Trends of the ET_a anomaly averaged over the entire
420 TP, the western TP, and the eastern TP are shown in Figure 7a. The domain
421 means of ET_a on the TP as a whole, and in the western TP decreased at rates
422 of -1.45 mm yr^{-1} and -5.52 mm yr^{-1} , respectively. However, the ET_a in the
423 eastern TP increased at a rate of 2.62 mm yr^{-1} . The decreasing rate of ET_a in
424 the entire TP is influenced mainly by the significant decrease of ET_a in the
425 western TP. Seasonally, the rates of change of ET_a over the whole TP are -
426 0.82 mm yr^{-1} ($p < 0.05$) and -0.79 mm yr^{-1} ($p < 0.05$) in spring and summer,
427 respectively (Figure 7b). However, in autumn and winter the ET_a changes at a
428 rate of 0.10 mm yr^{-1} and 0.06 mm yr^{-1} , respectively, and do not pass the t -test
429 ($p < 0.05$). ET_a in spring and summer seasons account for 75.7% of the
430 annual ET_a . The variation in amplitude and changing rates in these two
431 seasons are much larger than in the other seasons. Moreover, spatial
432 distributions of spring and summer ET_a trends are close to that of the annual
433 ET_a trend (Figure 6). Thus, changes of ET_a in the spring and summer
434 dominate the variations of ET_a in the whole year.

435

436 The decrease of ET_a over the whole TP and in the western TP during 2001-
437 2018 can be explained by the decrease of R_n in the same time period (Figure
438 8a). From 2001 to 2012, ET_a averaged over the entire TP increased slightly
439 and then decreased dramatically from 2012, reaching a minimum in 2014.
440 The significant decrease in ET_a between 2012 and 2014 was due to the rapid
441 decline of the R_n (Figure 8a). In the eastern TP, ET_a increased during 2001-
442 2018, while R_n decreased in the same period. Thus, R_n was not the dominant
443 factor controlling the annual variations of ET_a . However, the increasing trends
444 of both precipitation and air temperature can explain the increase of ET_a in the

445 eastern TP during the period 2001-2018 (Figure 8b and Figure 8c). The
446 increasing precipitation increased the water resource available for ET_a .
447 Moreover, the increasing air temperature accelerated the melting of
448 permafrost and glaciers on the TP. Hence, the melting water replenished the
449 ecosystem and increased the ET_a of the eastern TP.

450

451 Although the domain-averaged trend in ET_a has been decreasing across the
452 entire TP from 2001 to 2018, ET_a values in some areas have increased.
453 Moreover, the changing rates also depend on the time series of ET_a . For
454 example, the ET_a increased slightly from 2001 to 2012, while decreased from
455 2001 to 2018. This demonstrates the necessity to evaluate the spatial
456 distribution of changing trends in ET_a and utilize long time series to investigate
457 the trends in ET_a over the TP.

Formatted: Font: Italic

Formatted: Subscript

Deleted: high-spatial resolution datasets and

458 **4 Summary and conclusions**

459 The SEBS-estimated ET_a is at a resolution of around 10 km, while the
460 footprint of EC observed ET_a values ranges from a few dozen meters to a few
461 hundreds of meters. SEBS-estimated ET_a compares very well with
462 observations at the six flux towers, showing low RMSE and MB values. These
463 estimates were able to capture annual and seasonal variations in ET_a , despite
464 these two datasets being mismatched in their spatial representation.

465

466 Heterogeneous land surface characteristics and nonlinear changes in
467 atmospheric conditions resulted in heterogeneities in spatial distributions of
468 ET_a and changes in ET_a . The SEBS-estimated multiyear (2001-2018) mean
469 annual ET_a on the TP was 515 ± 22 mm, resulting in approximately
470 1287.5 ± 55.0 km³ yr⁻¹ of total water evapotranspiration from the terrestrial
471 surface. Annual ET_a generally decreased from the southeast to the northwest

473 of the TP. The maximum was over 1200 mm, in the southeastern Tibet and
474 Hengduan Mountains, while the minimum was less than 100 mm in the
475 northwest marginal area of the TP. Moreover, ET_a was typically lower than 200
476 mm over snow- and ice-bound mountainous areas, as there was limited
477 available energy to evaporate the water.

478

479 Averaged over the entire TP, annual ET_a increased slightly from 2001 to 2012,
480 but decreased significantly after 2012 and reached a minimum in 2014.

481 Generally, there was a slight decreasing trend in the domain mean annual ET_a
482 on the TP at the rate of -1.45 mm yr^{-1} ($p < 0.05$) from 2001 to 2018. However,
483 trends of annual ET_a were opposite in the western and eastern TP. The
484 annual ET_a decreased significantly in the western TP at a rate of -5.52 mm yr^{-1}
485 ($p < 0.05$) from 2001 to 2018, while annual ET_a in the eastern TP increased
486 at a rate of 2.62 mm yr^{-1} ($p < 0.05$) in the same period.

487

488 The spatial distributions of seasonal ET_a trends were also noticeably
489 heterogeneous during 2001-2018. The spatial patterns of ET_a trend in spring
490 and summer were similar to the annual changes in ET_a . ET_a decreased as
491 well in the spring and summer season but at slower rates compared with the
492 annual ET_a , however, only very weak trends were found in the autumn and
493 winter seasons.

494

495 5 Data availability

496 The dataset presented and analyzed in this article has been released and is
497 available for free download from the Science Data Bank
498 (<http://www.dx.doi.org/10.11922/sciencedb.t00000.00010>, (Han et al., 2020))
499 and from the National Tibetan Plateau Data Center

Deleted: rate of change of

Deleted: Finally,

502 (<https://data.tpdc.ac.cn/en/data/5a0d2e28-ebc6-4ea4-8ce4-a7f2897c8ee6/>).

503 The dataset is published under the Creative Commons Attribution 4.0
504 International (CC BY 4.0) license.

505

506 **Acknowledgments**

507 This study was funded by the Second Tibetan Plateau Scientific Expedition
508 and Research (STEP) program (grant no. 2019QZKK0103), the Strategic
509 Priority Research Program of Chinese Academy of Sciences (XDA20060101),
510 the National Natural Science Foundation of China (91837208, 41705005, and
511 41830650). The CMFD data were obtained from the National Tibetan Plateau
512 Data Center ([https://data.tpdc.ac.cn/en/data/8028b944-daaa-4511-8769-
513 965612652c49/](https://data.tpdc.ac.cn/en/data/8028b944-daaa-4511-8769-965612652c49/)). MODIS data were obtained from the NASA Land Processes
514 Distributed Active Archive Center (<https://lpdaac.usgs.gov/>). Global 1 km
515 forest canopy height data were obtained from the Oak Ridge National
516 Laboratory Distributed Active Archive Center for Biogeochemical Dynamics
517 (https://daac.ornl.gov/cgi-bin/dsviewer.pl?ds_id=1271). The authors would like
518 to thank all colleagues working at the observational stations on the TP for their
519 maintenance of the instruments.

520

521

- 523 Chen, X., Z. Su, Y. Ma, S. Liu, Q. Yu, Z. Xu. 2014. Development of a 10-year (2001-2010) 0.1° data set
524 of land-surface energy balance for mainland China. *Atmospheric Chemistry and Physics* 14(23):
525 13097-13117.
- 526 Chen, X., Z. Su, Y. Ma, E. M. Middleton. 2019. Optimization of a remote sensing energy balance method
527 over different canopy applied at global scale. *Agricultural and Forest Meteorology* 279: 107633-
528 107633.
- 529 Chen, X., Z. Su, Y. Ma, K. Yang, B. Wang. 2013a. Estimation of surface energy fluxes under complex
530 terrain of Mt. Qomolangma over the Tibetan Plateau. *Hydrol. Earth Syst. Sci.* 17(4): 1607-1618.
- 531 Chen, X., Z. Su, Y. Ma, K. Yang, J. Wen, Y. Zhang. 2013b. An Improvement of Roughness Height
532 Parameterization of the Surface Energy Balance System (SEBS) over the Tibetan Plateau. *Journal*
533 *of Applied Meteorology and Climatology* 52(3): 607-622.
- 534 Fisher, J. B., F. Melton, E. Middleton, C. Hain, M. Anderson, R. Allen, M. F. McCabe, S. Hook, D.
535 Baldocchi, P. A. Townsend, A. Kilic, K. Tu, D. D. Miralles, J. Perret, J.-P. Lagouarde, D. Waliser, A.
536 J. Purdy, A. French, D. Schimel, J. S. Famiglietti, G. Stephens, E. F. Wood. 2017. The future of
537 evapotranspiration: Global requirements for ecosystem functioning, carbon and climate feedbacks,
538 agricultural management, and water resources. *Water Resources Research* 53(4): 2618-2626.
- 539 Gao, Z. Q., C. S. Liu, W. Gao, N. B. Chang. 2011. A coupled remote sensing and the Surface Energy
540 Balance with Topography Algorithm (SEBTA) to estimate actual evapotranspiration over
541 heterogeneous terrain. *Hydrol. Earth Syst. Sci.* 15(1): 119-139.
- 542 Grant, A. L. M., P. J. Mason. 1990. Observations of boundary-layer structure over complex terrain.
543 *Quarterly Journal of the Royal Meteorological Society* 116(491): 159-186.
- 544 Han, C., Y. Ma, X. Chen, Z. Su. 2016. Estimates of land surface heat fluxes of the Mt. Everest region
545 over the Tibetan Plateau utilizing ASTER data. *Atmospheric Research* 168: 180-190.
- 546 Han, C., Y. Ma, X. Chen, Z. Su. 2017. Trends of land surface heat fluxes on the Tibetan Plateau from
547 2001 to 2012. *International Journal of Climatology* 37(14): 4757-4767.
- 548 Han, C., Y. Ma, Z. Su, X. Chen, L. Zhang, M. Li, F. Sun. 2015. Estimates of effective aerodynamic
549 roughness length over mountainous areas of the Tibetan Plateau. *Quarterly Journal of the Royal*
550 *Meteorological Society* 141(689): 1457-1465.
- 551 Han, C., Y. Ma, B. Wang, L. Zhong, W. Ma, X. Chen, Z. Su. 2020. The estimated actual
552 evapotranspiration over the Tibetan Plateau from 2001 to 2018. *VI. Science Data Bank.*
553 <http://www.dx.doi.org/10.11922/sciencedb.t00000.00010>.
- 554 He, J., K. Yang, W. Tang, H. Lu, J. Qin, Y. Chen, X. Li. 2020. The first high-resolution meteorological
555 forcing dataset for land process studies over China. *Scientific Data* 7(1): 25-25.
- 556 Immerzeel, W. W., L. P. H. van Beek, M. F. P. Bierkens. 2010. Climate Change Will Affect the Asian
557 Water Towers. *Science* 328(5984): 1382 LP-1385.
- 558 Li, X., G. Cheng, S. Liu, Q. Xiao, M. Ma, R. Jin, T. Che, Q. Liu, W. Wang, Y. Qi, J. Wen, H. Li, G. Zhu,
559 J. Guo, Y. Ran, S. Wang, Z. Zhu, J. Zhou, X. Hu, Z. Xu. 2013. Heihe Watershed Allied Telemetry
560 Experimental Research (HiWATER): Scientific Objectives and Experimental Design. *Bulletin of the*
561 *American Meteorological Society* 94(8): 1145-1160.
- 562 Li, X., L. Wang, D. Chen, K. Yang, A. Wang. 2014. Seasonal evapotranspiration changes (1983–2006)

563 of four large basins on the Tibetan Plateau. *Journal of Geophysical Research: Atmospheres* 119(23):
564 13,13-79,95.

565 Liu, X., H. Zheng, M. Zhang, C. Liu. 2011. Identification of dominant climate factor for pan evaporation
566 trend in the Tibetan Plateau. *Journal of Geographical Sciences* 21(4): 594-608.

567 Ma, N., J. Szilagyi, Y. Zhang, W. Liu. 2019. Complementary-Relationship-Based Modeling of Terrestrial
568 Evapotranspiration Across China During 1982–2012: Validations and Spatiotemporal Analyses.
569 *Journal of Geophysical Research: Atmospheres* 124(8): 4326-4351.

570 Ma, W., Y. Ma, H. Ishikawa. 2014. Evaluation of the SEBS for upscaling the evapotranspiration based
571 on in-situ observations over the Tibetan Plateau. *Atmospheric Research* 138: 91-97.

572 Ma, Y., Z. Hu, Z. Xie, W. Ma, B. Wang, X. Chen, M. Li, L. Zhong, F. Sun, L. Gu, C. Han, L. Zhang, X.
573 Liu, Z. Ding, G. Sun, S. Wang, Y. Wang, Z. Wang. 2020. A long-term (2005–2016) dataset of hourly
574 integrated land–atmosphere interaction observations on the Tibetan Plateau. *Earth Syst. Sci. Data*
575 12(4): 2937-2957.

576 Ma, Y., Z. Su, T. Koike, T. Yao, H. Ishikawa, K. i. Ueno, M. Menenti. 2003. On measuring and remote
577 sensing surface energy partitioning over the Tibetan Plateau—from GAME/Tibet to CAMP/Tibet.
578 *Physics and Chemistry of the Earth, Parts A/B/C* 28(1): 63-74.

579 Ma, Y., L. Zhong, B. Wang, W. Ma, X. Chen, M. Li. 2011. Determination of land surface heat fluxes over
580 heterogeneous landscape of the Tibetan Plateau by using the MODIS and in situ data. *Atmos. Chem.*
581 *Phys.* 11(20): 10461-10469.

582 Mauder, M., T. Foken. 2015. Eddy-Covariance Software TK3.

583 Moore, C. J. 1986. Frequency response corrections for eddy correlation systems. *Boundary-Layer*
584 *Meteorology* 37(1): 17-35.

585 Oki, T., S. Kanae. 2006. Global Hydrological Cycles and World Water Resources. *Science* 313(5790):
586 1068 LP-1072.

587 Pinker, R. T., I. Laszlo. 1992. Modeling Surface Solar Irradiance for Satellite Applications on a Global
588 Scale. *Journal of Applied Meteorology* 31(2): 194-211.

589 Shi, H., T. Li, G. Wang. 2017. Temporal and spatial variations of potential evaporation and the driving
590 mechanism over Tibet during 1961–2001. *Hydrological Sciences Journal* 62(9): 1469-1482.

591 Stull, R. B. (1988). An introduction to boundary layer meteorology. Dordrecht, Kluwer Academic
592 Publishers.

593 Su, Z. 2002. The Surface Energy Balance System (SEBS) for estimation of turbulent heat fluxes. *Hydrol.*
594 *Earth Syst. Sci.* 6(1): 85-100.

595 Szilagyi, J., R. Crago, R. Qualls. 2017. A calibration-free formulation of the complementary relationship
596 of evaporation for continental-scale hydrology. *Journal of Geophysical Research: Atmospheres*
597 122(1): 264-278.

598 Wang, B., Y. Ma, Z. Su, Y. Wang, W. Ma. 2020a. Quantifying the evaporation amounts of 75 high-
599 elevation large dimictic lakes on the Tibetan Plateau. *Science Advances* 6(26): eaay8558.

600 Wang, G., S. Lin, Z. Hu, Y. Lu, X. Sun, K. Huang. 2020b. Improving Actual Evapotranspiration
601 Estimation Integrating Energy Consumption for Ice Phase Change Across the Tibetan Plateau.
602 *Journal of Geophysical Research: Atmospheres* 125(3): e2019JD031799-e032019JD031799.

603 Wang, K., J. Liu, X. Zhou, M. Sparrow, M. Ma, Z. Sun, W. Jiang. 2004. Validation of the MODIS global
604 land surface albedo product using ground measurements in a semidesert region on the Tibetan

605 Plateau. *Journal of Geophysical Research: Atmospheres* 109(D5).

606 Webb, E. K., G. I. Pearman, R. Leuning. 1980. Correction of flux measurements for density effects due
607 to heat and water vapour transfer. *Quarterly Journal of the Royal Meteorological Society* 106(447):
608 85-100.

609 Xie, Z., Z. Hu, L. Gu, G. Sun, Y. Du, X. Yan. 2017. Meteorological Forcing Datasets for Blowing Snow
610 Modeling on the Tibetan Plateau: Evaluation and Intercomparison. *Journal of Hydrometeorology*
611 18(10): 2761-2780.

612 Xu, C. Y., V. P. Singh. 2005. Evaluation of three complementary relationship evapotranspiration models
613 by water balance approach to estimate actual regional evapotranspiration in different climatic
614 regions. *Journal of Hydrology* 308(1): 105-121.

615 Yang, K., H. Wu, J. Qin, C. Lin, W. Tang, Y. Chen. 2014. Recent climate changes over the Tibetan Plateau
616 and their impacts on energy and water cycle: A review. *Global and Planetary Change* 112: 79-91.

617 Yang, W., X. Guo, T. Yao, K. Yang, L. Zhao, S. Li, M. Zhu. 2011. Summertime surface energy budget
618 and ablation modeling in the ablation zone of a maritime Tibetan glacier. *Journal of Geophysical*
619 *Research: Atmospheres* 116(D14).

620 Yao, T., H. Lu, W. Feng, Q. Yu. 2019. Evaporation abrupt changes in the Qinghai-Tibet Plateau during
621 the last half-century. *Scientific Reports* 9(1): 20181-20181.

622 Yao, T., L. Thompson, W. Yang, W. Yu, Y. Gao, X. Guo, X. Yang, K. Duan, H. Zhao, B. Xu, J. Pu, A. Lu,
623 Y. Xiang, D. B. Kattel, D. Joswiak. 2012. Different glacier status with atmospheric circulations in
624 Tibetan Plateau and surroundings. *Nature Climate Change* 2(9): 663-667.

625 Zhang, C., F. Liu, Y. Shen. 2018a. Attribution analysis of changing pan evaporation in the Qinghai-
626 Tibetan Plateau, China. *International Journal of Climatology* 38(S1): e1032-e1043.

627 Zhang, K., J. S. Kimball, R. R. Nemani, S. W. Running. 2010. A continuous satellite-derived global
628 record of land surface evapotranspiration from 1983 to 2006. *Water Resources Research* 46(9).

629 Zhang, T., M. Gebremichael, X. Meng, J. Wen, M. Iqbal, D. Jia, Y. Yu, Z. Li. 2018b. Climate-related
630 trends of actual evapotranspiration over the Tibetan Plateau (1961–2010). *International Journal of*
631 *Climatology* 38(S1): e48-e56.

632 Zhang, Y., C. Liu, Y. Tang, Y. Yang. 2007. Trends in pan evaporation and reference and actual
633 evapotranspiration across the Tibetan Plateau. *Journal of Geophysical Research: Atmospheres*
634 112(D12).

635 Zhong, L., Y. Ma, Z. Hu, Y. Fu, Y. Hu, X. Wang, M. Cheng, N. Ge. 2019. Estimation of hourly land
636 surface heat fluxes over the Tibetan Plateau by the combined use of geostationary and polar-orbiting
637 satellites. *Atmos. Chem. Phys.* 19(8): 5529-5541.

638 Zhou, J., L. Wang, Y. Zhang, Y. Guo, D. He. 2016. Spatiotemporal variations of actual evapotranspiration
639 over the Lake Selin Co and surrounding small lakes (Tibetan Plateau) during 2003–2012. *Science*
640 *China Earth Sciences* 59(12): 2441-2453.

641 Zou, M., L. Zhong, Y. Ma, Y. Hu, Z. Huang, K. Xu, L. Feng. 2018. Comparison of Two Satellite-Based
642 Evapotranspiration Models of the Nagqu River Basin of the Tibetan Plateau. *Journal of Geophysical*
643 *Research: Atmospheres* 123(8): 3961-3975.

644

645

646 **List of tables**

647 Table 1: Input datasets used in this study. 23

648 Table 2: Station information. 24

649

650

651

652 Table 1: Input datasets used in this study.

Variables	Data source	Availability	Temporal resolution	Spatial resolution
Downward Shortwave	CMFD	1979 – 2018	3 hours	0.1°
Downward longwave	CMFD	1979 – 2018	3 hours	0.1°
Air temperature	CMFD	1979 – 2018	3 hours	0.1°
Specific humidity	CMFD	1979 – 2018	3 hours	0.1°
Wind velocity	CMFD	1979 – 2018	3 hours	0.1°
Land surface temperature	MOD11C3	2001 – now	Monthly	0.05°
Land surface emissivity	MOD11C3	2001 – now	Monthly	0.05°
Height of canopy	GLAS & SPOT	2000 - now	Monthly	0.01°
Albedo	MOD09CMG	2001 - now	Daily	0.05°
NDVI	MOD13C2	2001 - now	Monthly	0.05°
DEM	ASTER GDEM	-	-	30 m

653

654

655

656 Table 2: Station information.

Station	Location	Elevation (m)	Land cover
QOMS	28.21°N, 86.56°E	4276	Gravel
NAMORS	30.46°N, 90.59°E	4730	Grassy marshland
SETORS	29.77°N, 94.73°E	3326	Grass land
NADORS	33.39°N, 79.70°E	4264	Sparse grass-Gobi
MAWORS	38.41°N, 75.05°E	3668	Sparse grass-Gobi
BJ	31.37°N, 91.90°E	4509	Sparseness meadow

657

658

659

660 **List of figures**

661 Figure 1: Locations of the six flux tower sites (marked by pentagrams) on the
662 TP. The legend of the color map is elevation above mean sea level in meters.
663 26

664 Figure 2: SEBS-estimated and EC-observed monthly ET_a at the six stations (a-
665 f) on the TP in years when the latter observations were available. RMSE is the
666 root-mean-square error, MB is the mean bias, and R is the correlation
667 coefficient 27

668 Figure 3: Spatial distribution of the SEBS-estimated multiyear (2001-2018)
669 average annual ET_a 28

670 Figure 4: Spatial distributions of the SEBS-estimated multiyear (2001-2018)
671 average seasonal ET_a (mm/season) values over the TP. (a) spring, (b) summer,
672 (c) autumn, (d) winter. 29

673 Figure 5: Spatial distribution of annual ET_a linear trend on the TP from 2001 to
674 2018. The stippling indicates the trends that pass the t-test ($p < 0.05$). 30

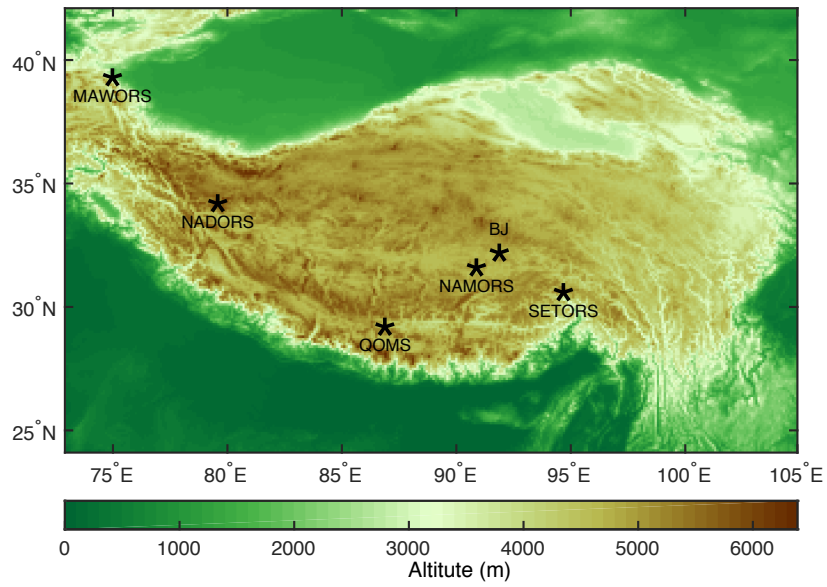
675 Figure 6: Spatial distributions of seasonal ET_a linear trends on the TP from 2001
676 to 2018: (a) annual, (b) spring, (c) summer, (d) autumn, (e) winter. The stippling
677 indicates the trends that pass the t-test ($p < 0.05$). 31

678 Figure 7: Anomalies of the domain-averaged annual ET_a of the entire TP, the
679 western TP ($\text{lon} < 90^\circ \text{ E}$), and the eastern TP ($\text{lon} > 90^\circ \text{ E}$), respectively (a).
680 Domain-averaged seasonal ET_a anomalies over the entire TP (b). The dashed
681 straight lines indicate linear trends during 2001-2018, and k is the slope of the
682 straight line. 32

683 Figure 8: Domain-averaged anomalies of annual R_n (a), precipitation (b), and
684 temperature (c) over the entire TP, the western TP ($\text{lon} < 90^\circ \text{ E}$), and the eastern
685 TP ($\text{lon} > 90^\circ \text{ E}$), respectively. The dashed straight lines indicate linear trends
686 during 2001-2018, and k is the slope of the straight line. 33

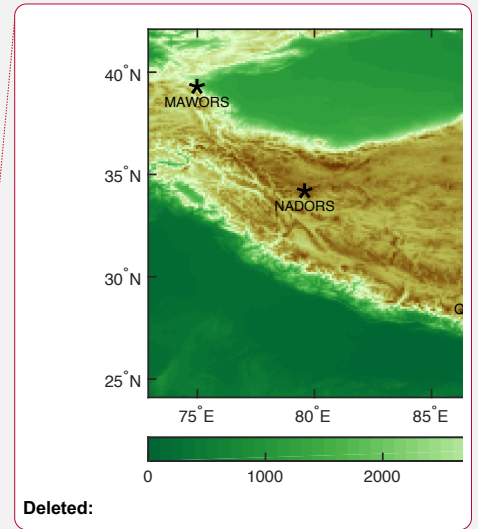
687

688

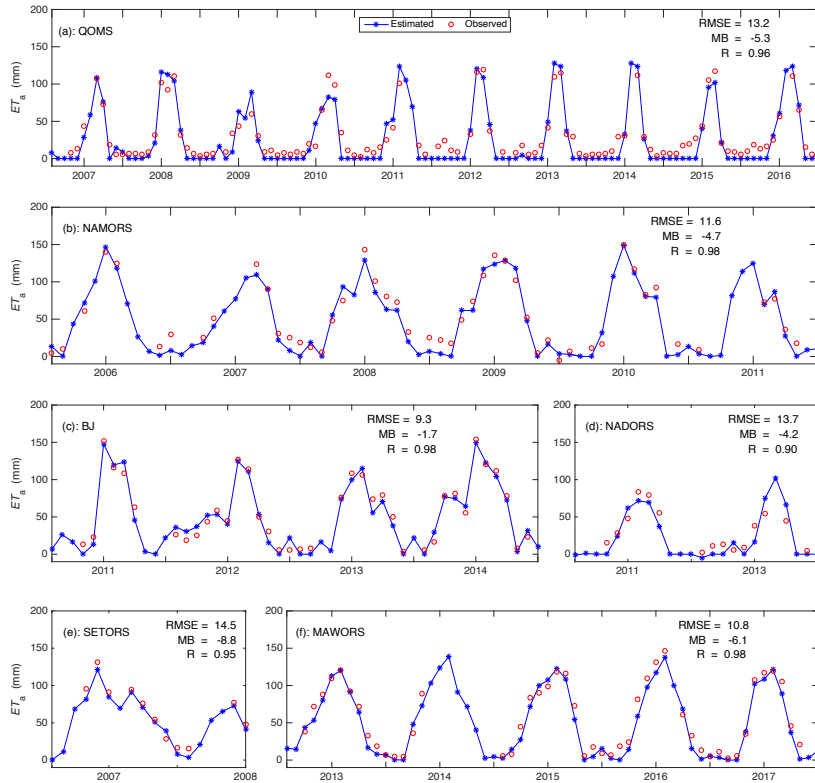


689

690 Figure 1: Locations of the six flux tower sites (marked by pentagrams) on the
691 TP. The legend of the color map is elevation above mean sea level in meters.
692



694

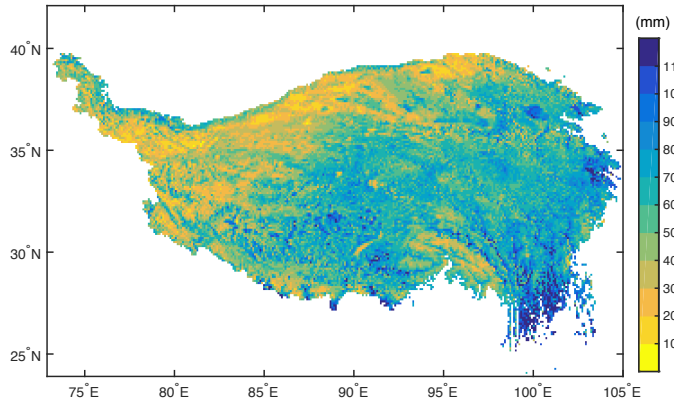


695

696 Figure 2: SEBS-estimated and EC-observed monthly ET_a at the six stations
697 (a-f) on the TP in years when the latter observations were available. RMSE is
698 the root-mean-square error, MB is the mean bias, and R is the correlation
699 coefficient.

700

701



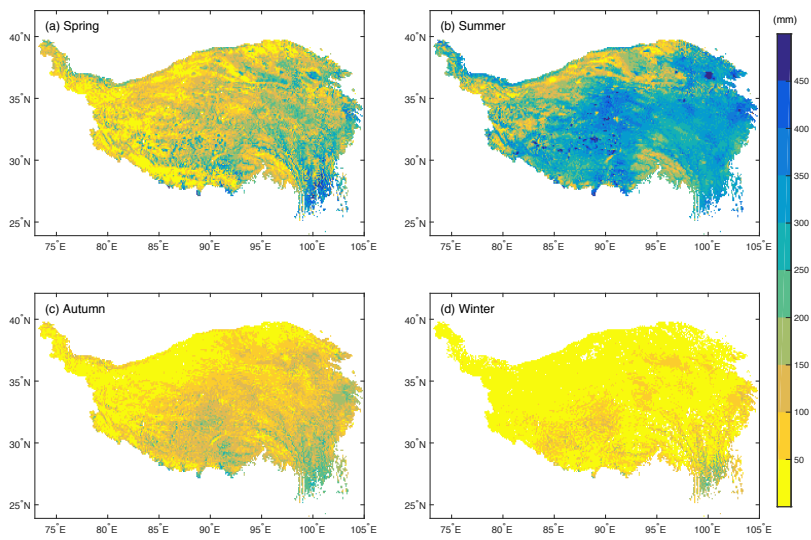
702

703 Figure 3: Spatial distribution of the SEBS-estimated multiyear (2001-2018)

704 average annual ET_a .

705

706



707

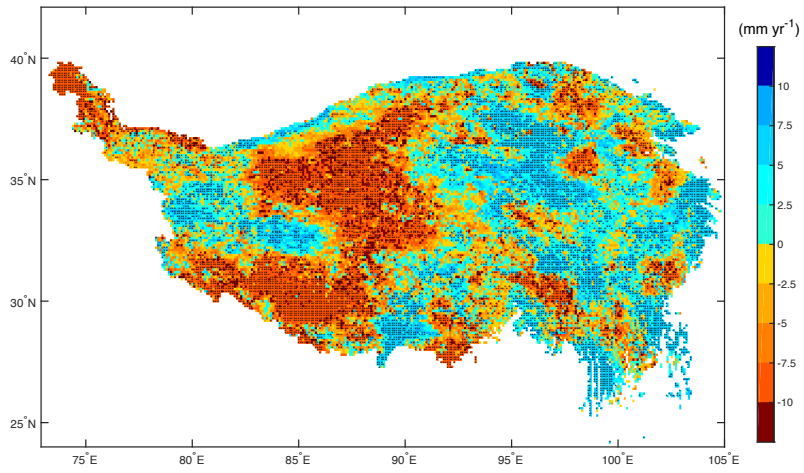
708 Figure 4: Spatial distributions of the SEBS-estimated multiyear (2001-2018)

709 average seasonal ET_a (mm/season) values over the TP. (a) spring, (b)

710 summer, (c) autumn, (d) winter.

711

712



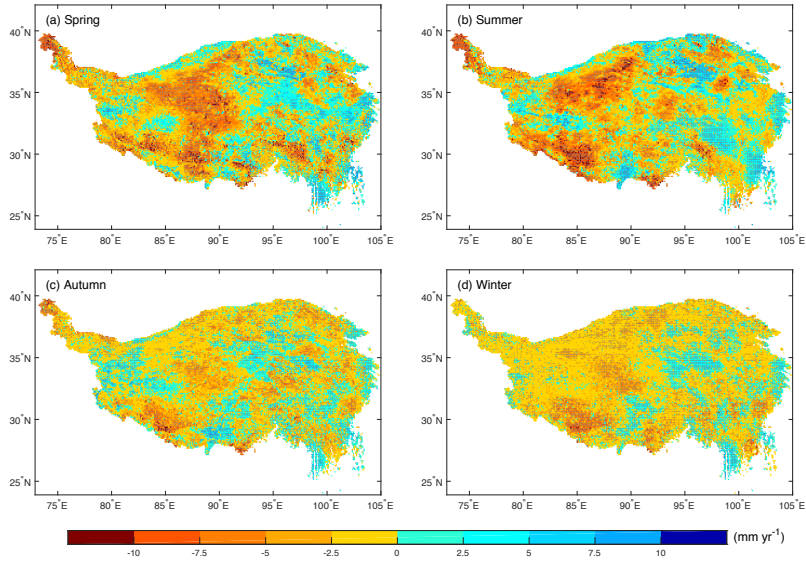
713

714 Figure 5: Spatial distribution of annual ET_a linear trend on the TP from 2001 to

715 2018. The stippling indicates the trends that pass the t-test ($p < 0.05$).

716

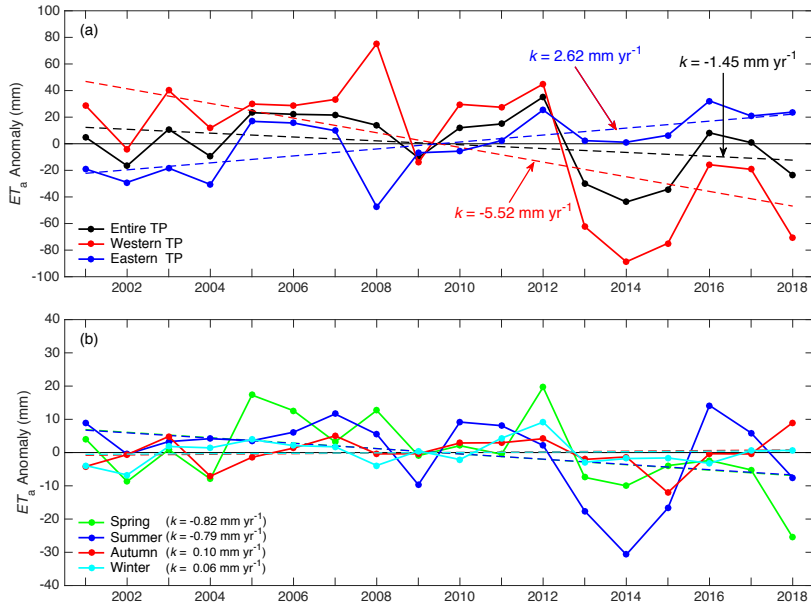
717



718

719 Figure 6: Spatial distributions of seasonal ET_a linear trends on the TP from
720 2001 to 2018: (a) annual, (b) spring, (c) summer, (d) autumn, (e) winter. The
721 stippling indicates the trends that pass the t -test ($p < 0.05$).
722

723



724

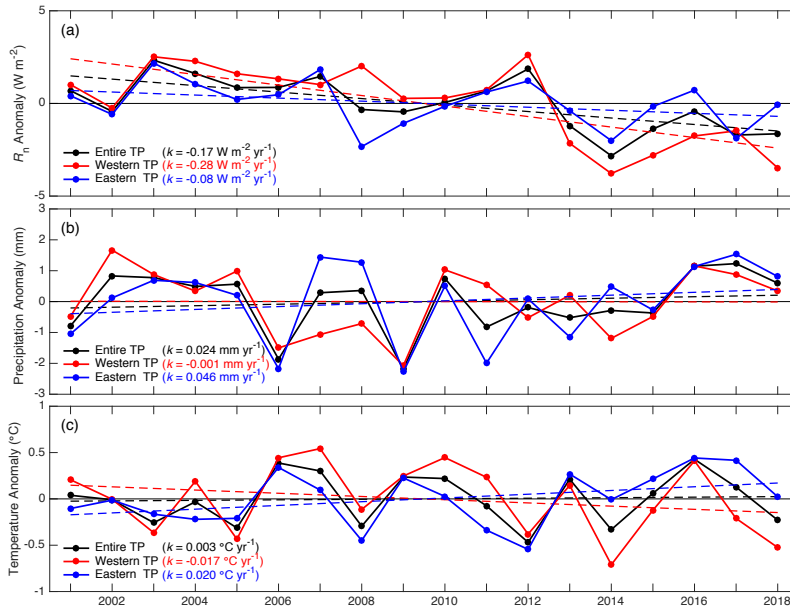
725 Figure 7: Anomalies of the domain-averaged annual ET_a of the entire TP, the
726 western TP (lon < 90° E), and the eastern TP (lon > 90° E), respectively (a).

727 Domain-averaged seasonal ET_a anomalies over the entire TP (b). The dashed
728 straight lines indicate linear trends during 2001-2018, and k is the slope of the
729 straight line.

730

731

732



733

734 Figure 8: Domain-averaged anomalies of annual R_n (a), precipitation (b), and

735 temperature (c) over the entire TP, the western TP ($lon < 90^{\circ} E$), and the

736 eastern TP ($lon > 90^{\circ} E$), respectively. The dashed straight lines indicate

737 linear trends during 2001-2018, and k is the slope of the straight line.

738